Type of the Paper (Article)

Design and Performance Evaluation of a Combined Edge-Film Lifting Mechanism for a Residual Film Recovery Machine

Haojun Wen [1,2,3], Haixiao Gou [1,2,3,*], Hao Chen [4], Zhaohui Zheng[1,2,3], Xiaolong Yang[1,2,3], Minhui Song[1,2,3] And Jie Zhang[1,2,3]

[1] College of Mechanical and Electrical Engineering, Shihezi University, Shihezi 832000, China; liyy@shzu.edu.cn (Y.L.);
[2] Key Laboratory of Northwest Agricultural Equipment, Ministry of Agriculture and Rural Affairs, Shihezi 832000, China
[3] Xinjiang Production and Construction Corps Key Laboratory of Modern Agricultural Machinery, Shihezi 832000, China
[4] Shanghai Huali Microelectronics Corporation, Shanghai 200000, China
* Correspondence: 994564712@qq.com;

Abstract: To address the challenge of ineffective flipping of the edge membrane, which affects subsequent recovery during residual film recovery, a modular edge membrane soil removal device was designed. The device consists of a trenching and soil removal unit, a membrane-lifting soil removal unit, and a "U"-shaped frame. Through theoretical calculations and mechanical analysis, the range values of key structural parameters—entry angle, rebate angle, and height difference—affecting its operational performance were determined. An EDEM simulation model for the edge membrane lifting device was established, and single-factor simulation experiments were conducted to narrow down the range of key parameters. Based on the results of the single-factor experiments, a second-order regression orthogonal rotational combination simulation experiment was conducted, using the entry angle, rebate angle, and height difference as experimental factors, and the soil removal rate and lift height as experimental indicators. Regression models for each experimental indicator and experimental factor were established, and the optimal structural parameter combination was determined. The experimental results show that the best operational performance occurs when the machine forward speed is 5.4 km/h, the entry angle is 33°, the rebate angle is 48°, and the height difference is 134 mm. At this point, the soil removal rate is 94.6%, and the lift height is 68.5 mm. To verify the performance of the optimized edge membrane lifting device, field experiments were conducted. The average soil removal rate was 92.38%, and the average lift height was 66.8 mm, which are in good agreement with the simulation theoretical values. The edge membrane recovery rate was 94.82%, which effectively increased the recovery rate of the edge membrane.

Keywords: residual film recovery; edge-film lifting device; discrete element simulation; parameter optimization; field experiment

1. Introduction

Plastic film mulching technology has been widely applied in agricultural production due to its advantages in warming the soil, conserving moisture, suppressing weeds, and increasing crop yield. This technology is particularly prevalent in cotton cultivation in the arid regions of Northwest China [1-4]. However, due to long-term heavy use and insufficient recycling, the issue of residual plastic film pollution has become increasingly serious. In this context, effective plastic film recovery has become an important issue that needs to be addressed in agricultural production.

Mechanical recovery has become the primary method of residual film recovery due to its high efficiency and low operational costs. During the plastic film mulching process, after the film is laid, a certain width of the edges on both sides of the film must be covered with soil and compacted. The portion of the film covered and fixed by soil is referred to as "edge film." Due to its burial depth, low strength, and tight bonding with the soil, mechanical recovery becomes difficult. Therefore, solving the effective recovery of edge film is the key to improving the overall film recovery rate [1,5].

The plastic film used in China is relatively thin and prone to aging and fragmentation. Relying solely on pulling the edge film makes recovery difficult. As a result, special edge film lifting devices are needed to break the bond between the film and soil, raising the edge film to the surface for easier recovery [6,7]. Scholars have conducted various studies on the structural optimization and operational performance of edge film lifting devices. Xie Jianhua[8] and others performed force analysis on three structures: spherical discs, double-wing shovels, and single-wing shovels. Based on the single-wing shovel design, they optimized it and validated its excellent soil-breaking effect in compacted soil through virtual simulation. Zhang Jiaxi [9] and others examined the integrity of the film lifting, soil removal rate, and soil accumulation phenomenon from the perspective of force characteristics. They pointed out that the entry angle and blade length significantly affect performance. Han Yingjie [10] and others analyzed the working conditions of edge film shovels at different soil entry depths through finite element analysis, studying the stress-strain states at 30 mm, 60 mm, and 90 mm entry depths. Hu Guangfa [11] and others designed a soil-breaking device consisting of a conical roller and soil-breaking blades, optimizing its structural parameters through simulation to enhance soil-breaking and film-lifting efficiency. Ma Shaohui [12] combined a toothed cutting film disc with a film-lifting shovel, enabling synchronous cutting and recovery of both edge and surface films. Furthermore, Jiang Yongxin [13] extended the design of surface film-lifting devices by adjusting shovel tooth parameters and establishing a film-to-soil interaction model, realizing integrated lifting of edge and surface films.

Although certain progress has been made in previous studies, most research still relies on traditional soil-contacting components, neglecting the complex coupling structure between the edge film and the soil. In particular, the curved structure of the bottom of the edge film tightly bonds with the soil, making it difficult to break and lift during operation, leading to low soil removal rate and inefficient recovery [6,10,14]. Therefore, in-depth study of the coupling characteristics of the edge film-soil structure, the construction of a simulation model based on real-world working conditions, and the design of devices based on this model are key to improving the recovery efficiency of edge film.

This study focuses on the autumn operation environment of cotton fields in Xinjiang, establishing a discrete element model of the edge film-soil structure. Based on this, a combined edge film soil removal device is designed to explore the impact of device structural parameters on the lifting effect, with field trials conducted to verify its applicability and reliability. The research results can provide theoretical support and technical pathways to improve the integrity of edge film lifting and promote the mechanized and efficient recovery of residual films.

2. Structure and Working Principle of the Edge Film Lifting Device

2.1. Structural Composition

As shown in Fig. 1, the edge film lifting device consists of three parts: the trenching and soil removal mechanism, the U-shaped frame, and the film-lifting and soil removal mechanism. The trenching and soil removal mechanism is located at the front of the entire device and is responsible for breaking up the soil structure in the arc-shaped bottom of the ridge. The film-lifting and soil removal mechanism is positioned higher than the trenching and soil removal mechanism and arranged on the opposite side at the rear. The front part of the shovel blade is connected to the vertical column, while the rear part is suspended, forming a hook-shaped groove flow structure at a certain angle with the vertical direction, which facilitates the lifting and flow of soil and edge film. The two mechanisms are connected by the U-shaped frame, with a certain space reserved in the structure to ensure that the soil on the film naturally falls into the pre-formed trench during the operation interval, thereby realizing a progressive collaborative working mode of "trenching—lifting."

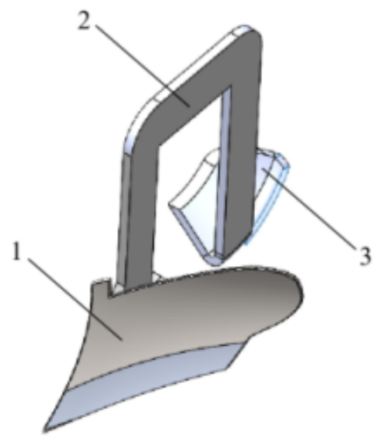

Figure 1. Schematic Diagram of the Edge-Lifting Film Device.

2.2. Working Principle

The working requirement of the edge film lifting device is to remove the soil covering the mulch film and effectively lift the edge film to the surface. The working process and principle are as follows: First, the trenching and soil discharge mechanism operates to excavate a trench on the side of the film arc at the bottom of the ridge using the three-wedge principle, flipping the soil within the trench to one side, which disrupts and destabilizes the soil-film structure at the bottom. Next, the bottom blade of the subsoil lifting device enters the soil to loosen the soil beneath the film arc. Subsequently, the back-hook type lifting and soil-discharge structure, while advancing, lifts the soil upward to the preset height, ensuring that the soil on the film naturally falls into the pre-dug trench during the lifting process, while effectively raising the edge film to the surface.

3. Design of Key Components and Determination of Parameters

3.1. Trenching and Soil Removal Mechanism

The working depth a and width b are the core parameters in the plow body curved surface design, which directly affect the soil disturbance effect and operational resistance [15–17]. To ensure sufficient soil fragmentation and smooth turnover during the film lifting operation, a reasonable matching must be achieved based on the conditions of soil instability and operational smoothness.

According to preliminary research and experiments, it was found that the arc part of the edge film in cotton fields is about 70 mm from the bottom of the ridge, with the soil thickness on the film not exceeding 90 mm. The soil texture in the working area is sandy loam, and the average soil compaction is 1754 kPa. Based on the soil anti-sliding stability coefficient $K=b/a$, it is required that $K\geq1.27$ under sandy loam conditions to achieve active soil breaking and effective soil removal. As shown in Fig. 2, by analyzing the relationship between the trench cross-sectional shape and area variation, the minimum trench area O_2 was determined to meet the volume transfer requirements of the soil on the film. Meanwhile, the plow body edge surface contour was optimized to reduce cutting resistance. The final working depth was determined as a=138 mm and width b=175 mm to meet the operational requirements for soil turnover, removal, and recovery in the edge film area.

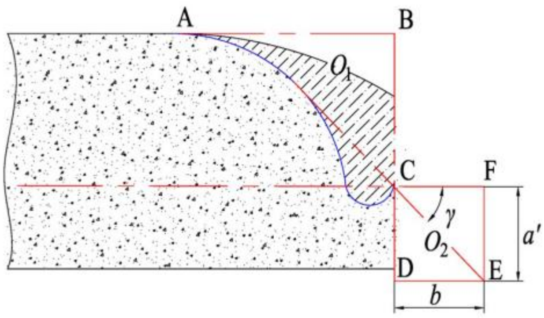

Figure 2. Collapse analysis

Fig. 3 shows the schematic diagram of the structural parameters of the plow body curved surface front view. The shape formed by points A, B, C, D, E, and F represents the outline of the plow body, while the quadrilateral PKLG indicates the theoretical outline of the lifted soil clod. The main parameters include the width b, the height of the shin blade line H, the maximum height of the top edge line H_{max}, the offset of the shin blade line Δx, the angle between the wing edge line δ, the overlap width between plowshares Δb, the parallel spacing Δs, and the height of the plowshare in the front view h.

The height deviation ΔH is set to 20 mm [16]. Since the trench wall has already been cut by the plow blade, to avoid scraping the trench wall, the shin blade line should be offset from the trench wall, with an offset Δx of 10 mm [17]. In the single plowshare design, the overlap width of the plowshares Δb=0, and the plow body height hs=115 mm. The parallel spacing Δs of the wing edge line EF is set to 10 mm [16]. In the edge film working environment, the maximum friction angle between sandy loam and 65Mn steel plowshares is φ_{max}=43.4°, and the calculated plowshare angle θ_0=47°. As shown in Eq. 5, the plowshare height h is calculated to be 50 mm. When the working depth a<180 mm, the soil at the bottom of the clod becomes more adhesive, so the height deviation ΔH is taken as a positive value [18]. The final calculations give the wing edge line angle δ=52°, the shin blade line height H=175 mm, and the maximum height of the top edge line H_{max}=243 mm.The formulas for the calculation of each parameter are shown in Eqs. (1-5):

$$H=b \tag{1}$$

$$H_{max}=\sqrt{a^2+b^2}\pm\Delta H \tag{2}$$

$$\delta = arcsin\,(a/b) \tag{3}$$

$$h = h_s\, sin\,\theta_0 \tag{4}$$

$$\theta_0 = \frac{\pi}{2} - \varphi_{max} \tag{5}$$

In the equation, H represents the shin blade height (mm), H_max is the maximum height of the top edge line (mm), and ΔH is the height deviation (mm). δ denotes the wing edge line included angle (°), while h is the plowshare height (°), and h_s is the length of the shin blade line on the plowshare (mm). θ_0 is the plowshare angle (°), and φ_max is the maximum friction angle between the soil and the plowshare (°).

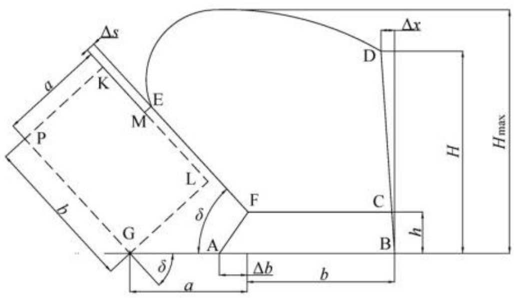

Figure 3. Cross-Sectional Diagram of the Plow Furrow.

The variation law of the plowshare angle θ_0 to θ_{min} for the semi-spiral trenching plow is generally assumed to follow a straight line. The corresponding plowshare angles are calculated proportionally using the linear Eqs. (6-7).

$$y_{line} = x\frac{\theta_0 - \theta_{min}}{58} + \theta_0 \tag{6}$$

$$m_{line} = \frac{\theta_0 - \theta_{min}}{2} \tag{7}$$

Table 1. Angle of straight-line partial line.

Area	Straight Line Segment			
Z/mm	0	16.7	33.3	50
Plowshare Angle θ (°)	47°	46°	45°	44°

The variation between θ_{min} and θ_{max} follows a parabolic pattern [16-22], which can be expressed by Eq. (8). According to the agricultural design handbook, the values of θ_{min} and θ_{max} are selected as 44° and 57°, respectively. A two-dimensional coordinate system is established with θ_{min} as the origin, as shown in Fig. 4. The horizontal axis x represents the height Z of the plowshare between θ_{min} and θ_{max}, in centimeters; the vertical axis y represents the ratio of the angle θ. First, the corresponding y-values for x are calculated, and then θ-values are converted based on Eqs. (10-11). The Z-value corresponding to θ_{min} is 50 mm, and the Z-value corresponding to θ_{max} is 243 mm.

$$y_{parabola} = \frac{x^2}{2P} \tag{8}$$

$$x = Z_{max} - Z_{min} \tag{9}$$

$$m_{parabola} = \frac{(\theta_{max} - \theta_{min})2P}{y_{max} - y_{min}} \tag{10}$$

$$\theta_{Element\ Line} = \theta_{min} + m y_{\mathrm{parabola}} \tag{11}$$

Where P is the intermediate variable; the x-axis represents the element line number; Z_{min} corresponds to the height at θ_{min}.

Table 2. Parabolic partial element line angle.

Area	Parabolic Part					
x/mm	0	38.6	77.2	115.8	154.4	193
my	0	0.52°	2.08°	4.68°	8.32°	13°
Element Line Angle θ(°)	44°	44° 32'	46° 5'	48° 41'	52° 19'	57°

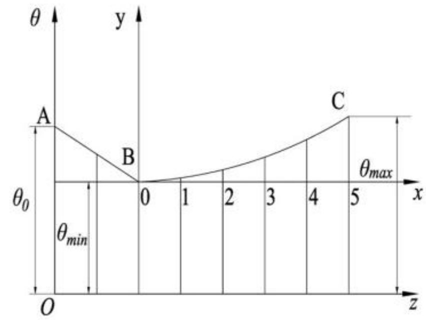

Figure 4. Variation Law of the Generatrix Angle in the Furrowing and Soil-Discharging Device.

The guiding curve is located within the vertical plane N-N, which is perpendicular to the plowshare. When the position of the vertical plane on the plowshare changes, different surface shapes are formed, thereby affecting the surface performance. The edge film lifting device and the trenching and soil removal mechanism are responsible for soil turning. For the soil-turning type plow, the N-N plane is located at a distance L from the plow tip [22]. In addition, the dimensions and shape of the parabolic guiding curve are determined by the guiding curve height H_d, opening size L, plowshare mounting angle ε, starting line length S, and the angle ω between the tangents at both ends of the parabolic curve.

When the guiding curve height is fixed, the smaller the opening size, the steeper the curve, and the stronger the soil-breaking ability. Therefore, the L value for soil-turning type plows is smaller, which helps improve soil breaking efficiency. The opening size is related to the plow size. For a working width less than 250 mm, L is set to 1750 mm. The larger the plowshare mounting angle ε, the stronger the soil-breaking ability. Based on the reference, ε is set to 25°. The starting line length is proportional to the working depth. When the edge film lifting device operates at a shallow depth, S is set to 30 mm. The tangent angle ω is calculated according to Eq. (12). To facilitate the turnover of the soil clod, the upper part of the guiding curve can be twisted forward, increasing the angle $\Delta\varepsilon$ between the tangent at the upper endpoint and the vertical line [15-21]. The guiding curve height needs to satisfy the condition $H_{max} > H_d > H$, and can be calculated using Eq. (13). The schematic diagram of the guiding curve is shown in Fig. 5.

$$\omega=90°+\varepsilon-\Delta\varepsilon \tag{12}$$

$$H_d=C_hL \tag{13}$$

The value of $\Delta\varepsilon$ is set to 10°, and C_h is set to 1.6 [15–23].

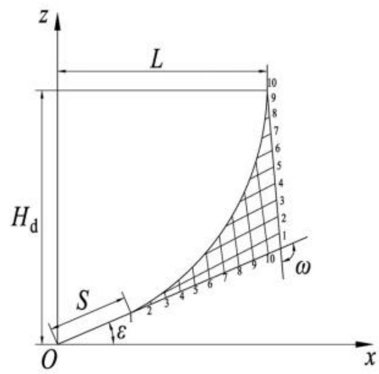

Figure 5. Schematic Diagram of the Guide Curve.

3.2. Design of the Under-Mulch Soil Lifting and Removal Device

To avoid tearing the membrane and affecting the recovery efficiency due to the symmetrical structure, the under-mulch soil lifting and removal mechanism adopts a single-sided soil entry and inward hook design. This structure not only prevents membrane damage but also enables effective soil disturbance beneath the membrane and smooth lifting of the edge film, meeting the requirements for complete edge film recovery.

Assuming the soil entry angle is α_n, the force on the conventional wing plow is shown in Fig. 6. Its equilibrium equation [23] is given by Eq. (14):

$$P = N\sin\alpha_n + f\cos\alpha_n + R \tag{14}$$

In the equation, P is the traction force (N); f is the friction force between the soil and the edge membrane lifting device ($f = \mu N$, N); N is the normal load exerted by the soil on the wedge surface (N); R is the cutting resistance on the wedge surface ($R = KB$, N); α_n is the angle between the wedge surface and the ground (°); B is the blade width of the edge membrane lifting device (mm); K is the cutting resistance per unit blade width (N); and N and f represent the sum of all the infinitesimal forces acting on the entire shovel surface (N).

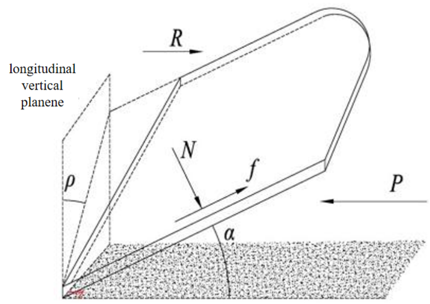

Figure 6. Force Principle Diagram of the Retractable Wing Shovel Penetrating into Soil.

The under-mulch soil lifting and removal device adopts a hooked-wing plow structure. It has been determined that the working width of this structure is the distance from the top of the edge film soil structure to the outermost part of the arc, approximately 90 mm. During steady forward motion, the hooked-wing plow is divided into multiple infinitesimal surfaces by its cross-section, and force analysis is performed on each infinitesimal surface, as shown in Fig. 7. After the hooked-wing plow enters the soil at a certain angle, it lifts the soil upwards along the surface of the plow wing and conveys it backward, eventually falling into the side soil guiding trench. During the soil entry operation of the hooked-wing plow, due to its small front width, the cutting resistance is negligible. The forces mainly concentrate in the forward direction [23–25]. The mutual relationship is shown in Eq. (15):

$$P_1 = N_2\sin\varphi + f_2\cos\varphi + f_1\cos\alpha + (N_1 + T_1)\sin\varphi \tag{15}$$

In the equation, f_1 is the frictional force on the wedge surface of the rebate wing plow due to soil ($f_1 = \mu N_1$, N); f_2 is the frictional force on the wedge surface of the rebate wing plow due to soil ($f_2 = \mu N_2$, N); P_1 is the traction force (N); N_1 is the normal load on the surface of the rebate wing plow (N); N_2 is the soil pressure exerted on the cutting edge of the rebate wing plow (N); α is the entry angle (°); φ is the angle between the cutting edge of the rebate wing plow and the forward direction (shear angle) (°); T_1 is the internal frictional force in the soil (N).

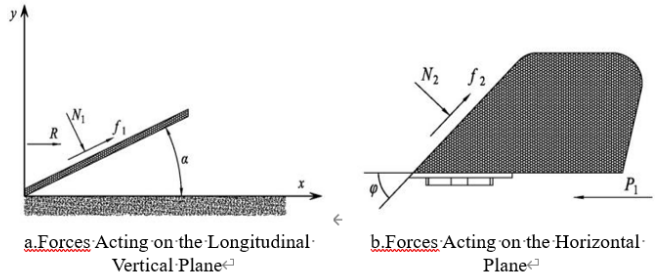

Figure 7. Spatial Force Diagram of the Sub-Mulch Lifting and Soil-Removing Device.

During the soil entry operation of the hooked-wing plow, the soil forces are shown in Fig. 7. Similarly, Eq. (16) can be derived.

$$\begin{cases} N_1 \sin\varphi - N_3 \sin\theta' + f_1 \cos\alpha - (F_1 + T_1 + F_{\alpha 1}) \cos\theta' = 0 \\ G - N_1 \cos\alpha + f_1 \sin\alpha + N_3 \cos\theta' + (F_1 + T_1 + F_{\alpha 1}) \sin\theta' = 0 \end{cases} \tag{16}$$

In the equation, B is the width of the rebate wing plow (m); T_1 is the internal frictional force in the soil (N), where $T_1 = \mu' N_3$; F_1 is the shear force when the soil internal shear failure occurs (N), where $F_1 = cS$ (S is the shear surface area of the soil clod); G is the weight of the soil clod (N); Fa_1 is the accelerating force that causes soil movement (N), where $Fa_1 = \gamma/g\ Bdv^2 \cdot sin(\alpha)/sin(\alpha+\theta)$; N_3 is the pressure exerted by the surface soil on the rebate wing plow surface (N); and θ' is the soil shear surface inclination angle (°).

From Eqs. (15-16), the traction force P_1 is given by Eq. (17):

$$P_1 = N_2(\sin\varphi + \mu\cos\varphi) + \frac{\mu\cos\alpha + \sin\alpha}{g\sin(\alpha+\theta')} \times$$

$$\frac{G\sin(\alpha+\theta')(\sin\theta' + \mu'\cos\theta') + cSg\sin(\alpha+\theta') + YBDv^2\sin\alpha}{(1-\mu\mu')\sin(\alpha+\theta') + (\mu+\mu')\cos(\alpha+\theta')} \tag{17}$$

Through computational analysis, it is found that as the soil entry angle α of the hooked-wing plow increases, the working resistance of the plow also increases, and the interaction force between the plow and the soil in front of it becomes greater, which is beneficial for soil compression, breaking, and lifting. As the entry angle increases, the soil is more easily heaped and lifted [26]. Typically, α should be less than 38°, but due to the soil support in front of the lifted soil clod, it can be appropriately increased beyond 38° [16]. The range of α can be taken from 15° to 40°. To reduce the soil entry resistance, the angle φ between the plow's blade and the forward direction is typically set to 30° according to the Agricultural Machinery Design Handbook [16].

To prevent tearing the edge film or excessive soil accumulation, which would increase operational resistance, the sum of the projection length and height difference of the plow wing in the vertical plane must not exceed the soil entry depth of the opening and soil removal device. According to the principle of limits, the length B' of the plow wing is influenced by both the height Δh and the soil entry angle α, and their geometric relationship is shown in Fig. 8, which can be calculated using Eq. (18).

$$B'\cos\alpha = 175 - \Delta h \tag{18}$$

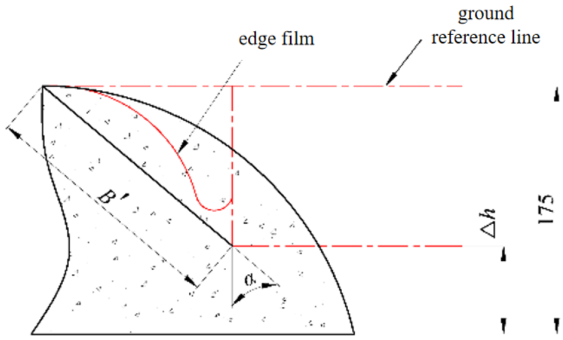

Figure 8. Analysis of shovel wing soil height.

In the figure, Δh is the height difference between the cutting edges of the two working components; B' is the width of the plow wing; α is the soil entry angle.

3.3. Design of U-shaped Connecting Frame

The U-shaped connecting frame not only serves to connect the two structural parts but also ensures the required height difference between them. The gap in the middle of the U-shaped structure is designed to ensure that, when the under-mulch soil lifting and removal device has not yet operated, the soil on the film has enough time to naturally fall into the trench after the opening and soil removal device operates. Assuming the soil on each square decimeter of the film behaves as a whole, after the trenching operation, the soil will naturally fall into the trench due to its own weight. Based on the previous data, the soil falls to a depth of 138 mm, with a mass of 350 g/dm^2 per square decimeter. Using $s = 0.5at^2$, the free fall time for the soil is calculated to be 0.17 s. Considering the forward speed of the residual film recovery machine is 5.4 km/h, the required gap distance is calculated to be 257 mm, rounded to 260 mm.

3.4. Motion Trajectory Analysis

3.4.1. Analysis of Soil Motion Trajectory During the Edge Film Lifting Process

The combined edge film soil removal device adopts a progressive film lifting operation process. First, the trenching and soil removal mechanism breaks the soil at the bottom of the ridge's arc, then the under-film soil lifting mechanism loosens and lifts the soil by hooking. The two mechanisms use a semi-spiral trenching plow and a hooked-wing plow structure, both of which can be likened to a combination of multiple three-sided wedges. The entire operation process can be seen as the collaborative action of a dual three-sided wedge system. A three-dimensional Cartesian coordinate system is established, where the forward directions of the two parts are along the x-axis, and the hooking soil turnover direction is along the y-axis, both of which discharge the soil to one side. The z-axis is perpendicular to the *xoy* plane and follows the soil lifting direction, as shown in Fig. 9. Here, Δh is the height difference between the cutting edges of the two working components; A-F and A1-F1 are the vertices of the two three-sided wedges; δ' is the angle between C1D1 and D1F1. The main structural angles include the soil entry angle α, the soil turnover angle β, and the pushing angle δ. In the established three-dimensional coordinate system, the x-axis represents the forward direction, the y-axis represents the soil discharge direction, and the z-axis represents the soil lifting direction. The under-film device rotates positively around the x-axis towards the y-axis to form the hooking angle ρ, with the structural angle relationships shown in Fig. 7.

$$\tan\alpha = \tan\beta \tan\delta \tag{19}$$

$$\tan\beta = \tan\lambda \tan\delta \tag{20}$$

$$\tan\alpha = \tan\lambda \tan\delta \tag{21}$$

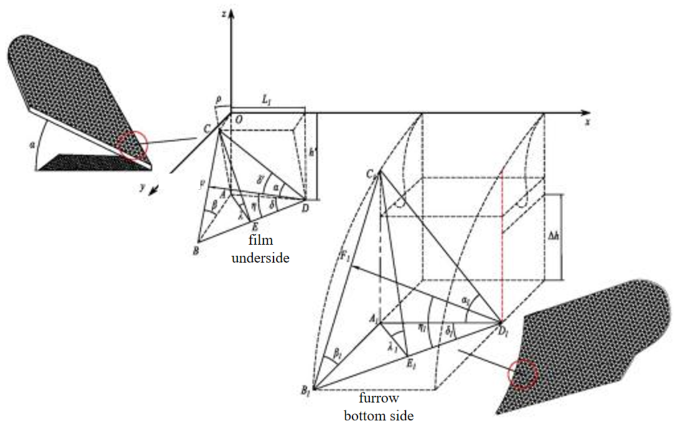

Figure 9. Micro element analysis of soil disturbance of combined edge film dumping device.

The soil trajectory line can be used to predict the direction of soil movement along the wedge surface. According to Goryachkin's soil fragmentation theory and the minimum energy theory by Mukoguchi, the direction of soil particles' movement on the wedge surface is consistent with the direction of the force component when the wedge body moves forward. As shown in Fig. 7, the angle between DF and DB on the wedge surface is η, which characterizes the direction of soil particles entering the wedge surface. Its magnitude determines the direction of the soil trajectory line. Based on the mechanical and geometric relationships during the operation process, the soil trajectory line angle satisfies the following relation: $\tan\eta = \cos\lambda\tan\delta$.

3.4.2. Analysis of Soil Trajectory Line in the Trenching and Soil Removal Mechanism

Based on the design parameters mentioned earlier, the soil entry angle and the wedge angle of the trenching plow in the trenching and soil removal mechanism have been determined. From this, the corresponding soil trajectory line angle η at each moment can be further calculated. By combining Fig. 9 and constructing the equation of the intersection line between the trenching plow's surface and the *yoz* plane (Eq. 22), and using the known point D1($H\cot\alpha_1 + L_1 + 210100$, $-$ H), the spatial equation of the plow surface can be derived (Eq. 23).

$$\begin{cases} y = -x\tan\rho\theta_0 + L_1 + 210 \\ z = 0 \end{cases},\ \ y \in [0, L_2\sin\theta_0] \tag{22}$$

$$(y + 90) + z\cot\theta_0 + (x + L_1 + 210)\cot\alpha_1 = 0 \tag{23}$$

In the equation, L_1 is the longitudinal length of the rebate wing plow (mm); L_2 is the initial element straight line length (mm); and θ_0 is the initial angle of the horizontal element straight line (°).

Based on the geometric relationship of the three-sided wedge, the soil trajectory line equation is established as shown in Eqs. (24-25).

$$H = h' + \Delta h \tag{24}$$

$$\begin{cases} x = \left(H\cot\alpha_1 + L_1\cos\dfrac{\theta_0}{2}\right)t + H\cot\alpha_1 + L_1 + 210 \\ y = -L_1 t\sin\dfrac{\theta_0}{2} + 90 \\ z = -tH - H \\ A = \dfrac{2H\sin\delta'}{\sin\alpha_1\sin\eta_1} \end{cases} \tag{25}$$

In the equation, h is the soil entry depth (mm); Δh is the height difference between the tips of the two working components (mm); δ' is the angle between C_1D_1 and D_1F_1 (°); and t is an intermediate variable.

3.4.3. Analysis of Soil Trajectory Line in the Under-film Soil Lifting and Removal Mechanism

By combining Fig. 6, Fig. 7, and Fig. 9, the equation of the hooked-wing surface of the under-film soil lifting and removal mechanism, passing through the straight line L_3, can be derived using Eq. (26). The equation of the hooked-wing surface passing through the straight line L_3 and point D ($h'\cos\rho\cot\alpha$, 0, -h') can then be determined by Eqs. (27).

$$\begin{cases} z = -y\tan\rho \\ x = 0 \end{cases},\ \ y \in [0,\ B\sin\rho] \tag{26}$$

$$\tan\alpha x - \sin\rho y + \cos\rho z = 0 \tag{27}$$

In the equation, B is the width of the plow wing (mm); ρ is the hooking angle (°).

Based on the geometric relationship of the three-sided wedge, the soil trajectory line equation is established as shown in Eqs. (28-29).

$$\Delta h = 17 - h' \tag{28}$$

$$\begin{cases} x = \tan\alpha t \\ y = -t\sin\rho + L_3\cos\rho \\ z = \cos\rho t - L_3\sin\rho \\ L_3 = \dfrac{h'\sin\rho\sin\delta''}{\sin\alpha\sin\eta} \end{cases} \tag{29}$$

In the equation, L_3 is the length of the intersection line between the plow surface and the *yoz* plane (mm); δ'' is the angle between CD and DF (°); t is an intermediate variable.

Comprehensive analysis shows that the soil entry angle α, hooking angle ρ, and soil entry depth h' are key parameters affecting the disturbance effect on the soil and the soil movement trajectory of the hooked-wing plow. When α is small, the vertical disturbance force is insufficient, which is not conducive to soil loosening and the lifting of the edge film. As α increases, together with ρ, a spatial inclined surface structure is formed, enhancing the lateral compressive force of the soil, promoting its sliding along the bottom of the trench, and effectively preventing accumulation. According to the agricultural machinery design specifications, combined with the edge film structure and the positioning constraints of the U-shaped frame, the operational width is determined to be 100 mm. The parameter relationship $100B\sin\rho$=100 is derived, and $\rho \in$ (0°–90°) is constrained. Additionally, the upper and lower limits of the soil entry depth h' should meet the requirements of preventing membrane damage and not exceeding the trenching depth. Its value is closely related to the cutting edge height difference Δh and has a decisive impact on the soil movement trajectory. Therefore, the soil entry angle α, hooking angle ρ, and height difference Δh are selected as the three-factor variables for structural optimization, aiming to design a combined edge film soil removal device to achieve the purpose of lifting the edge film.

3.5. Determination of Installation Position and Analysis of Necessary Conditions for Edge Film Recovery

Based on previous research findings and the residual film recovery operation process, the device has two layout modes: The first is to lift the film before the straw crushing device. This method causes less interference and has low resistance, but the film may be covered again by straw after lifting, which is not conducive to subsequent recovery. The second is to lift the film after the straw crushing device and before the recovery mechanism. Although the operational resistance slightly increases, it effectively avoids obstruction by straw. After comprehensive consideration, this paper adopts the second layout method. According to the agronomic requirements of double-sided film covering, the edge film lifting device is symmetrically arranged on both sides of the machine, with the installation position shown in Fig. 10.

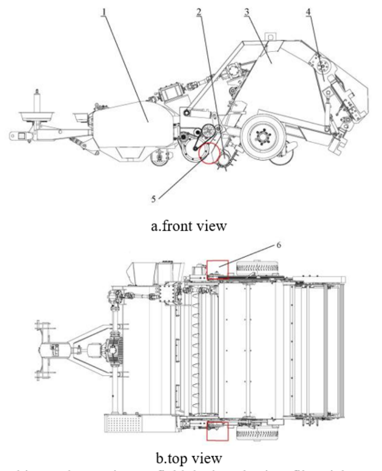

1.Straw crushing and returning-to-field device Plastic 2.film pickup mechanism 3.Film detachment device 4.Film rolling device 5、6. Installation positions of edge-lifting devices

Figure 10. Tooth chain residual film recovery machine.

The tooth-chain type picking device picks up and conveys the edge film using nail teeth. To ensure its normal operation, the motion trajectory of the device needs to be analyzed to determine the minimum height at which the edge film must be lifted. The motion of the nail teeth is a combination of uniform circular motion around the rotation center and horizontal linear motion in the direction of the machine's advancement. Taking the rotation center O of the nail teeth as the origin, a two-dimensional coordinate system is established (with xxx as the direction of the machine's advancement and y as the vertical direction), as shown in Fig. 11.

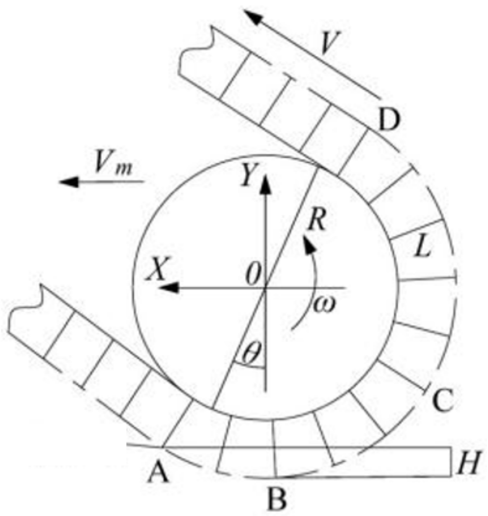

Figure 11. Spur tooth trajectory diagram.

Based on the geometric relationship, the motion trajectory equation of the nail teeth endpoint C is given by Eq. (30).

$$\begin{cases} X_C = V_m \times t + (R+L) \times \sin\left(\theta + \frac{V}{R+L} t\right) \\ Y_C = -(R+L) \times \cos\left(\theta + \frac{V}{R+L} t\right) \end{cases} \tag{30}$$

In the equation, R is the radius of the conveyor chain track (m); V_m is the machine's forward speed ($m \cdot s^{-1}$); L is the length of the nail teeth (m); t is the machine's forward time (s); V is the film pickup and conveying speed ($m \cdot s^{-1}$); θ is the angle between the initial soil entry point of the nail teeth and the Y-axis (°).

In the measurements, the rotational radius R = 128 mm, forward speed V_m = 5.4 km/h, conveying speed V = 6.9 km/h, and the nail teeth soil entry depth is 30 mm. According to Eq. (31), the nail teeth motion trajectory is stable, and the trajectory height of the nail teeth endpoint can be predicted. Therefore, to ensure that the edge film enters the pickup trajectory smoothly, the design should ensure that the minimum lifting height of the film's arc is no less than 50 mm to meet the requirements of the film recovery machine.

4. Simulation Analysis and Optimization

4.1. Establishment and Analysis of the Simulation Model

4.1.1. Establishment of the Simulation Model

To accurately reconstruct the geometric shape of the edge film in the soil and improve modeling efficiency, this study uses the Meta-Particle function in EDEM software to generate the edge film structure. First, the spatial coordinate distribution of the edge film particles must be determined. The HyperMesh software is used to mesh the edge film structure and extract the residual film node coordinate information. This data is then imported into EDEM software, where the Meta-Particle function is used to directly generate a surface edge film model that conforms to the geometric distribution characteristics of the soil layer, as shown in Fig. 12.

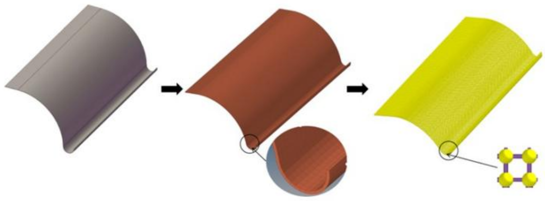

Figure 12. Coordinate acquisition and edge film model establishment.

Since the soil moisture content is not uniformly distributed, and to simulate the actual soil environment, the approach in references [27-28] is adopted. The soil is divided into three layers based on moisture content: 10.0%, 16.0%, and 25.0%, with the corresponding soils prepared for each moisture content (Fig. 13a). The discrete element model of the edge film-soil structure is constructed in three steps. First, a three-layer subsoil structure is generated based on the soil parameters under the film, and a complete three-dimensional soil-film structure model is established by considering the spatial distribution of the edge film in the soil layers and the overall shape of the soil-film structure. The second step is to improve modeling efficiency by directly generating the surface edge film model above the soil-film structure and allowing it to fall into the pre-designed groove. The third step involves generating soil particles above the model according to the previously measured soil mass parameters, completing the overall modeling of the soil-film structure system, as shown in Fig. 13.

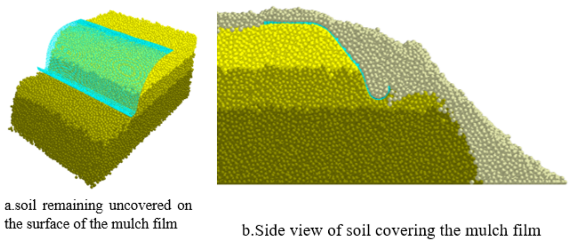

Figure 13. Discrete element model of edge film soil structure.

4.1.2. Simulation Parameter Settings

To simplify the simulation model and reduce computational complexity, this study discretizes the macroscopically continuous edge film structure and treats it as a composition of single-layer particles bonded together. The particles are not allowed to overlap, and only tangential constraints and the shear force generated by them are considered. According to references [29-31], the normal stiffness of the bonding bonds between particles is related to the material's elastic modulus and Poisson's ratio, and the tangential stiffness K_s =1/3 nK. Therefore, when setting the parameters, it is sufficient to set the normal and tangential stiffness between the edge film particles to be the same. Considering that the molecular scale of the film material is too small for direct modeling, a scaling process is applied, and the radius of the edge film particles is uniformly set to 1 mm. The intrinsic parameters and contact parameters of the edge film in the model are shown in Table 3.

Table 3. EDEM simulation parameters of edge film particles.

Parameter	Value	Source
Poisson's ratio	0.44	
Elastic modulus	1.72×10^8 Pa	[28]
Density	915 kg/m^3	
Coefficient of restitution	0.86	
Static friction coefficient	0.52	[29][30]
Kinetic friction coefficient	0.43	

Under the condition of a maximum soil moisture content of 25%, the unit width bond force between the soil and the edge film is only 0.0007 N/mm, which is extremely small and can be ignored in the modeling process. Furthermore, the bond force between the edge film and soil with lower moisture content can also be considered negligible. Since the soil on the edge film is generally in a dry and loose state, and due to the impact of the cotton harvester's wheel compaction, the soil structure is fragmented and its compactness is reduced, the contact force between the film and the soil mainly exhibits conventional non-bonding contact behavior. Therefore, the contact behavior between the soil on the film, the soil beneath the film, and the edge film is uniformly described using the Hertz-Mindlin contact model. The relevant contact parameters are set based on literature data, as detailed in Table 4.

Table 4. EDEM simulation parameters of soil on film and edge film-soil particles.

Parameter	Value	Source
Collision restitution coefficient of soil particles on the film	0.48	[13][31]
Static friction coefficient of soil particles on the film	0.56	
Kinetic friction coefficient of soil particles on the film	0.24	
Collision restitution coefficient of 65Mn steel and soil particles on the film	0.5	
Static friction coefficient of 65Mn steel and soil particles on the film	0.31	
Kinetic friction coefficient of 65Mn steel and soil particles on the film	0.1	
Collision restitution coefficient of the edge film and soil particles	0.25	[32][33]
Static friction coefficient of the edge film and soil particles	0.24	
Kinetic friction coefficient of the edge film and soil particles	0.18	
Collision restitution coefficient of 65Mn steel and edge film particles	0.1	
Static friction coefficient of 65Mn steel and edge film particles	0.25	
Kinetic friction coefficient of 65Mn steel and edge film particles	0.05	

4.1.3. Simulation Model Validation

To verify the rationality of the constructed membrane-soil structure model, penetration resistance tests were conducted. By setting up a penetration probe in the simulation platform that is consistent with the field tests, the force variations during the probe's penetration into the membrane arc structure were recorded. The simulation results indicated that the maximum force on the probe was 9.67 N, which is only a 4.7% error compared to the field-measured value of 10.12 N. This validates the accuracy of the established discrete element model in terms of mechanical response and the reliability of the simulation results, providing a basis for subsequent parameter optimization and performance simulations.

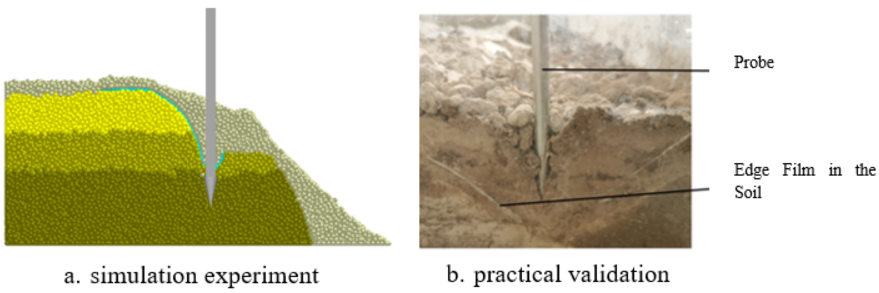

Figure 14. Section of penetration resistance test.

4.1.4. Analysis of the Operation Process of Edge Film Lifting Device

The operation process of the edge film lifting device is shown in Fig. 15. Under the action of the trenching and soil-throwing device, the edge film-soil structure begins to loosen, and the bottom soil of the ridge is thrown backward (Fig. 15(a)). As the machine advances, the soil under the film and the edge film are lifted by the soil lifting device under the film. The soil under the film flows into the excavated trench along the buckle direction from the suspended end of the shovel wing, and the edge film arc gradually unfolds. The original interlocking structure is gradually destroyed, and the soil on the film falls through the gap in the "U"-shaped connection frame during the lifting process (Fig. 15(b)). The soil mass on the film is significantly reduced, and the edge film is lifted to a certain height and suspended on the soil surface, completely destroying the interlocking structure (Fig. 15(c)).

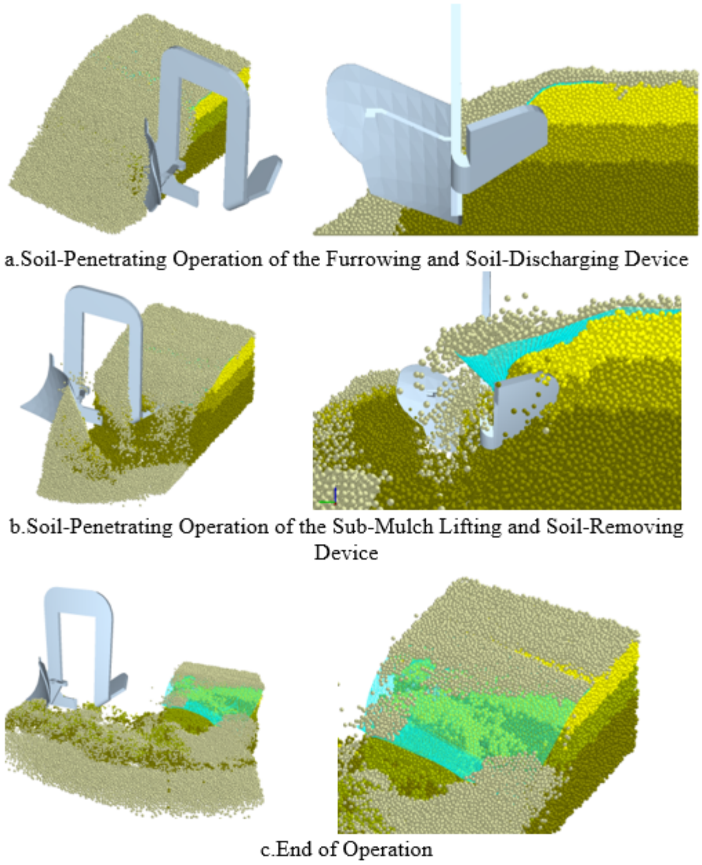

Figure 15. Simulation Test of the Edge-Lifting Film Device and Its Behavior at Different Time Intervals.

4.2. Single-factor Simulation Test

Based on the previous analysis, the range of the entry angle α is 15°-40°, the rebate angle ρ is 24°-56°, and the height difference Δh is 90-150 mm. A single-factor experiment is conducted to explore the effects of entry angle, rebate angle, and height difference on the soil removal rate and lifting height, in order to narrow down the parameter range. According to Eq. (31), the soil removal rate in the simulation test is defined based on the relationship between the residual soil on the membrane and the input soil mass. The lifting height is measured from the lowest point of the membrane's arc, and the height difference before and after the simulation is calculated.

$$y=1-\frac{Z_y}{Z_c} \tag{31}$$

In the equation, y is the soil removal rate, Z_y is the remaining soil particle mass (g), and Z_c is the total input soil particle mass (g).

4.2.1. Analysis of the Effect of Insertion Angle

Based on the reference [9] and actual operating conditions, the backhaul angle was set at 40° and the height difference between the two components was set to 120 mm. The soil removal rate after the operation of the edge film removal device was measured under different insertion angles. A total of 10 experimental groups were tested, each repeated 3 times, and the average value of the 3 tests was taken. The impact of the backhaul angle on soil removal rate and lifting height is shown in Figure 16.

As shown in Fig. 16, with the increase in insertion angle, the soil removal rate gradually increases. When the insertion angle increases from 15° to 30°, the soil removal rate changes relatively slowly; however, when the insertion angle increases from 30° to 34°, the soil removal rate significantly rises, with an increase of 30%. This is because, with other conditions remaining constant, a larger insertion angle intensifies the vertical disturbance of the soil, thereby improving the soil lifting capacity. This not only benefits the lifting and spreading of the edge film, but also helps the soil on the film to lift and fall into the pre-dug trench, destroying the interlocking structure and increasing the soil removal rate. As the insertion angle increases, the lifting height also gradually increases. This is because the increase in insertion angle causes the vertical action angle to gradually approach the soil's internal friction angle, enhancing the soil's fluidity and facilitating soil lifting. Therefore, in the multi-factor experimental design, the range of insertion angles is set between 21° and 34°.

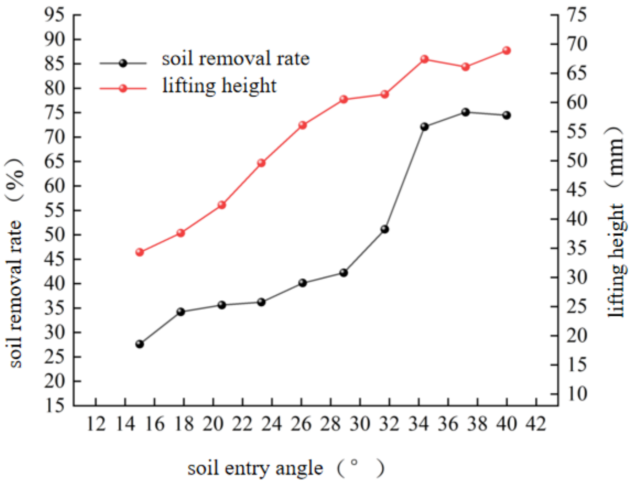

Figure 16. Soil Removal Efficiency at Different Entry Angles.

4.2.2. Analysis of the Impact of the Reversal Angle

A single-factor experiment was conducted based on reference [9] and actual conditions. When the soil entry angle was set at 27.5° and the height difference between the two parts was 120 mm, the soil removal rate after the operation of the edge film device was measured for different reversal angles. The test consisted of 10 groups, with each group repeated 3 times. The average of the 3 test results was taken. The effect of the reversal angle on the soil removal rate and lifting height is shown in Fig. 17.

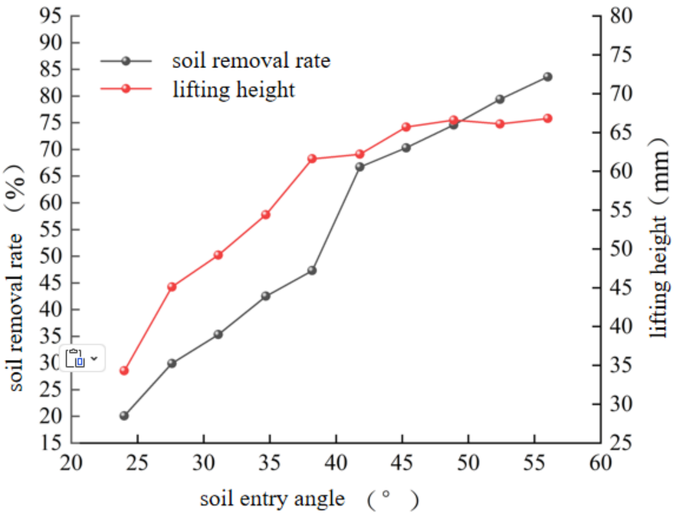

Figure 17. Soil Removal Efficiency at Different Folding Angles

With the increase of the reversal angle, the soil removal rate generally shows an upward trend, with a significant leap observed when the reversal angle reaches approximately 40°. The reason is that, under the condition that other factors remain constant, the gradual increase in the reversal angle enhances the disturbance to the soil inside the plow wing, thus expanding both the overall range and intensity of soil disturbance. When the reversal angle approaches 40°, the soil removal rate increases to 19.4%. As the reversal angle increases, the lifting height also increases and tends to stabilize around 45°, with the lifting height approximately 75 mm. Therefore, in the multi-factor experiment, the reversal angle is centered around 40°, and the range of values for the reversal angle is set between 32° and 48°.

4.2.3. Height Difference Impact Analysis

Based on reference [9] and combined with actual conditions, a single-factor test was conducted. When the entry angle was set at 27.5° and the rollback angle at 40°, the soil removal rate after the edge film device operation was measured under different height differences. The test was carried out in 10 groups, with each group repeated 3 times, and the average of the three test results was taken. The influence of different height differences on the soil removal rate and elevation height is shown in Fig. 18.

The results are shown in Fig. 18. As the height difference increases, the soil removal rate continues to rise. The reason for this is that under constant conditions, based on the collapse analysis mentioned earlier, the trenching and soil removal device first enters the soil to create a trench. On one hand, it clears the soil at the bottom of the ridge, reducing its inhibitory effect on the falling soil on the film. On the other hand, it creates a certain height difference, causing the slope angle to exceed the natural internal friction angle of the soil, thus promoting the sliding of the soil on the film. As the height difference increases, the slope angle formed becomes larger, making it easier for the soil on the film to slide down. As a result, when the subsequent soil lifting device operates, the remaining soil on the film decreases, which helps in effectively lifting the edge film.

Fig. 18 shows that when the height difference is in the range of 95-105 mm, there is a sudden change in elevation height, increasing sharply from 35 mm to 50 mm. This is because, at smaller height differences, the distance between the shovel wing and the arc section is too close, and the disturbance space formed between the rollback wing plow and the shovel wing is too narrow, unable to effectively lift the edge film. This leads to the film accumulating at the front and making it difficult to spread smoothly. As the height difference further increases, the disturbance space enlarges and moves away from the arc area, making it easier to lift the soil while successfully spreading the edge film. When the height difference reaches 135 mm, the growth trend of the lifting height begins to stabilize. Therefore, in the multi-factor test, the height difference range was set between 105 and 135 mm.

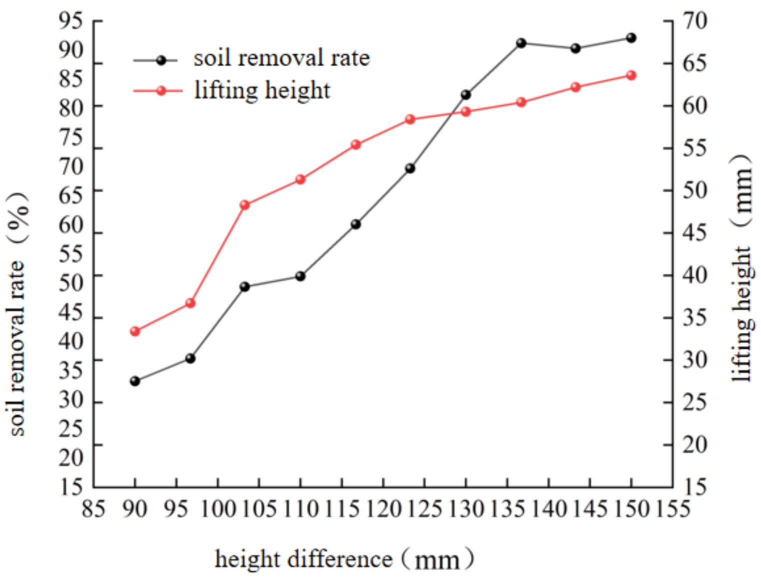

Figure 18. Soil Removal Efficiency at Different Height Differences.

4.3. Multi-factor Simulation Optimization Test

4.3.1. Experimental Design

Based on the results of the single-factor experiments, it is observed that the rebate angle, entry angle, and height difference all have a significant impact on the operational performance of the edge film removal device. To further investigate the effects of structural parameters and their interactions on the performance indicators, a three-factor quadratic regression orthogonal rotational combination experiment [33,35] is conducted to obtain the optimal combination of structural parameters. The level coding of each experimental factor is shown in Table 5.

480 **Table 5.** Factor Level Coding Table.

Coding	A - Entry Angle (°)	B - Rebate angle (°)	C - Height Difference (mm)
-1.68179	21	32	105
-1	24.25	36	112.5
0	27.5	40	120
+1	30.75	44	127.5
+1.68179	34	48	135

481 The arrangement of the simulation experiments and data results are shown in Table 6.

482 **Table 6.** Design Scheme and Results of a Three-Factor Quadratic Regression Orthogonal Rotatable Combination Design.

Serial Number	A - Entry Angle (°)	B - Rebate angle (°)	C - Height Difference (mm)	Soil Removal Rate (%)	Lifting Height (mm)
1	-1	-1	-1	33.43	51.2
2	1	-1	-1	44.56	59.7
3	-1	1	-1	24.12	56.2
4	1	1	-1	50.04	63.7
5	-1	-1	1	46.08	53.9
6	1	-1	1	49.32	67.3
7	-1	1	1	58.68	54.2
8	1	1	1	94.22	68.3
9	-1.6817	0	0	26.68	52.1
10	1.68179	0	0	59.48	68.9
11	0	-1.68179	0	32.25	54.7
12	0	1.68179	0	80.79	61.5
13	0	0	-1.68179	28.76	50.3
14	0	0	1.68179	72.21	62.2
15	0	0	0	33.6	56.9
16	0	0	0	39.84	59.1
17	0	0	0	41.8	60.9
18	0	0	0	34.92	56.6
19	0	0	0	37.72	56.5
20	0	0	0	36.28	55.7
21	0	0	0	47.98	55.7
22	0	0	0	29.84	56.7
23	0	0	0	30.12	57.1

483 4.3.2. Soil Removal Rate Influence Analysis

484 (1) Regression Model for Soil Removal Rate

485 Using Design-Expert software, the experimental data were analyzed, and a quadratic regression model for the soil removal rate Y_1 was established (Eq. (32)). The analysis of variance (ANOVA) results (Table 7) show that the model is highly significant with $P<0.0001$, and the P-value for the lack of fit is 0.3068 (> 0.05), indicating that the model fits well and the experimental data are reliable. Further analysis of the P-values for each factor and their interaction terms reveals

that the entry angle *A*, the return angle *B*, the height difference *C*, and the interaction between the return angle and height difference *BC* all have highly significant effects on the soil removal rate (P < 0.01). The interaction between the entry angle and return angle *AB*, the quadratic term of the return angle B^2, and the quadratic term of the height difference C^2 have significant effects (0.01 < P < 0.05). However, the interaction between the entry angle and height difference *AC*, as well as the quadratic term of the entry angle A^2, do not significantly affect the soil removal rate (P > 0.05). According to the F-values for each factor in the table, the influence of the factors on the soil removal rate is ranked as follows: height difference > return angle > entry angle.

$$
\begin{aligned}
Y_1 &= 36.92+9.95A+9.91B+12.39C+5.98AB \\
&+0.2163AC+7.67BC+2.06A^2+6.87B^2+4.64C^2
\end{aligned}
\tag{32}
$$

Table 7. Analysis of Variance (ANOVA) Table for Soil Removal Efficiency.

Variation Source	Sum of Squares	Degrees of Freedom	Mean Square	F	P
Model	6567.43	9	729.71	18.68	< 0.0001**
A - Entry Angle	1256.45	1	1256.45	32.16	< 0.0001**
B - Rebate angle	1340.52	1	1340.52	34.32	< 0.0001**
C - Height Difference	2096.88	1	2096.88	53.68	< 0.0001**
AB	277.18	1	277.18	7.10	0.0195*
AC	0.3741	1	0.3741	0.0096	0.9235
BC	470.17	1	470.17	12.04	0.0042**
A^2	65.20	1	65.20	1.67	0.2189
B^2	729.84	1	729.84	18.68	0.0008**
C^2	342.63	1	342.63	8.77	0.0110*
Residua	507.84	13	39.06		
Lack of Fit	240.75	5	48.15	1.44	0.3068
Error	267.10	8	33.39		
Total	7075.28	22			

(2) Response Surface Analysis of Soil Removal Rate

The analysis results indicate that the interaction between the entry angle and the rebate angle (AB) and the interaction between the rebate angle and the height difference (BC) have a significant effect on the soil removal rate. Therefore, these two sets of interaction factors were selected for response surface analysis.

Under the condition of a fixed height difference of 120 mm, the response surface of the interaction between the entry angle (A) and the rebate angle (B) is shown in Fig. 19(a). When the rebate angle remains constant, Y_1 shows a positive correlation with the entry angle, increasing as the entry angle increases. Conversely, when the entry angle is fixed, Y_1 also increases as the rebate angle increases. This trend is consistent with the results of the single-factor experiment, verifying the reliability of the model. Comprehensive analysis of the surface shape and contour distribution indicates that the optimal working performance of the edge membrane device occurs when the entry angle is between 27° and 34°, and the rebate angle is between 44° and 48°. Furthermore, the interaction between these two factors is most significant.

Fig. 19(b) shows the impact trend of the interaction between the rebate angle (B) and the height difference (C) on Y_1 under the condition of a fixed entry angle of 27.5°. When the entry angle remains constant, the value of Y_1 increases with the increase in both the rebate angle and height difference, which is consistent with the results of the single-factor experiment. Comprehensive analysis of the surface shape and contour distribution shows that when the rebate angle is between 32° and 48°, and the height difference is between 125 mm and 135 mm, the soil removal rate reaches a high level, indicating that the interaction between these two factors is significant within this range.

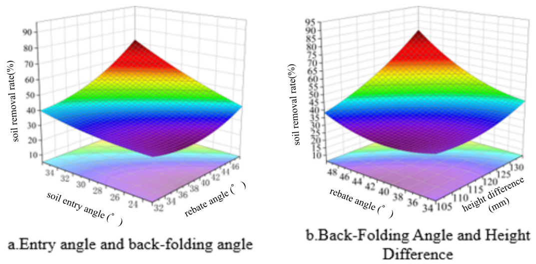

Figure 19. Response Surface Plot of Soil Removal Efficiency

4.3.3. Analysis of the Impact of Lift Height

(1) Regression Model for Lift Height

The experimental data were analyzed using Design-Expert software, and a quadratic regression model for lift height (Y_2) was constructed (Eq. (33)). The results of the analysis of variance are shown in Table 7. The model is highly significant with $P < 0.0001$, and the lack of fit is not significant ($P = 0.3674 > 0.05$), indicating that the model fits well and the experimental data are highly reliable.

Further analysis of the P values for each factor and their interaction terms reveals that the entry angle (A), rebate angle (B), height difference (C), the interaction between the entry angle and height difference (AC), and the quadratic term of the entry angle (A^2) all have a highly significant impact on lift height ($P < 0.01$). However, the interaction terms AB (entry angle and rebate angle), BC (rebate angle and height difference), the quadratic term of the rebate angle (B^2), and the quadratic term of the height difference (C^2) do not significantly affect the lift height ($P > 0.05$).

Based on the F-values of the factors in the table, the order of their influence on lift height is as follows: entry angle > height difference > rebate angle.

$$Y_2=57.22+5.25A+1.59B+2.41C-0.0375AB+1.44AC \\ -0.9625BC+1.35A^2+0.5028B^2-0.1513C^2 \quad (33)$$

Table 8. Analysis of Variance (ANOVA) Table for Lifting Height.

Variation Source	Sum of Squares	Degrees of Freedom	Mean Square	F	P
Model	548.19	9	60.91	19.29	< 0.0001**
A - Entry Angle	377.00	1	377.00	119.40	< 0.0001**
B - Rebate angle	34.60	1	34.60	10.96	0.0056**
C - Height Difference	79.32	1	79.32	25.12	0.0002**
AB	0.0113	1	0.0113	0.0036	0.9533
AC	16.53	1	16.53	5.24	0.0395*
BC	7.41	1	7.41	2.35	0.1495
A^2	29.02	1	29.02	9.19	0.0096**
B^2	4.02	1	4.02	1.27	0.2797
C^2	0.3635	1	0.3635	0.1151	0.7398
Residua	41.05	13	3.16		
Lack of Fit	18.06	5	3.61	1.26	0.6457
Error	22.98	8	2.87		
Total	589.23	22			

(2) Response Surface Analysis of Lift Height

The analysis indicates that the interaction between the entry angle (*A*) and the height difference (*C*) (*AC*) has a significant impact on the lift height (Y_2), thus response surface analysis is conducted.

When the rebate angle is 40°, the response surface of the interaction between the entry angle (*A*) and the height difference (*C*) on the lift height (Y_2) is shown in *Fig. 19*. When the height difference is constant, the lift height (Y_2) increases as the entry angle increases, showing a positive correlation. Similarly, when the entry angle is constant, the lift height (Y_2) is positively correlated with the height difference. These trends are consistent with the conclusions from the single-factor experiment.

Based on the contour and response surface analysis results in *Fig. 20*, it can be concluded that the maximum lift height is achieved when the entry angle is between 32° and 33.75°, and the height difference is between 115 mm and 135 mm. At this point, the interaction between the two factors is most significant.

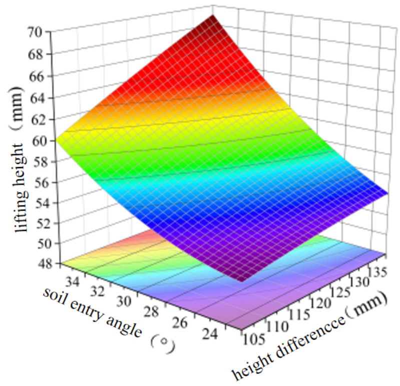

Figure 20. Response Surface Plot of Lifting Height

3.3.4. Parameter Optimization and Validation

This study aims to improve the soil removal rate and lift height by selecting the optimal configuration of key structural parameters to achieve better operational performance. The optimization of multi-factor experimental parameters was carried out using the optimization solving function of Design-Expert software. Under the premise of satisfying the experimental range of each factor, both the soil removal rate (Y_1) and the lift height (Y_2) are maximized. The mathematical model is established as shown in Equation 34.

$$\begin{cases} \max Y_1 \\ \max Y_2 \\ -1.68179 \leq A \leq +1.68179 \\ -1.68179 \leq B \leq +1.68179 \\ -1.68179 \leq C \leq +1.68179 \end{cases} \quad (34)$$

By combining the objective function and constraint conditions mentioned above, the regression equation of the experimental factors with respect to the soil removal rate was optimized, yielding the optimal solution: When the forward speed of the machine is 5.4 km/h, the entry angle (α) is 33°, the rebate angle (ρ) is 48°, and the height difference (Δh) is 134 mm. The soil removal rate is 94.6%, and the lift height is 68.5 mm. At this point, the soil remaining on the membrane is 18.9 g/dm², which is less than 125 g/dm², and the lift height is greater than 50 mm, meeting the design requirements.

5. Field Experiment Validation

5.1. Experimental Plan and Methods

To validate the operational performance of the edge membrane soil removal device under the optimal parameter combination, field experiments were conducted using the optimal combination obtained from the optimization process. Specifically, when the forward speed of the machine is 5.4 km/h, the entry angle (α) is 33°, the rebate angle (ρ) is 48°, and the height difference (Δh) is 134 mm. Each experimental trial covered a distance of 50 m, and the edge membrane experiment was repeated 10 times.

For each membrane, three large sampling points of 2050 × 1000 mm were randomly selected. Each large sampling point was divided into 10 smaller sampling points of 200 × 200 mm. After sampling, an electronic scale was used to determine the soil mass on each small membrane section. The average soil mass on the membrane before the experiment was calculated. After the experiment, the same sampling method was used to measure the remaining soil on the membrane. The soil removal rate was then calculated using Equation (33).

For the lift height measurement, a black marker was used to mark the lowest point of the membrane arc before the experiment. After the experiment, a height vernier caliper was used to measure the position of the black endpoint. The height difference was calculated, and the average value was obtained.

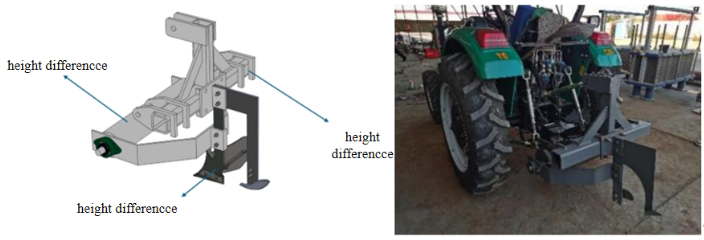

Figure 21. 3D Model and Physical Photograph of the Combined Edge Film Soil-Discharging Device.

In order to prove that the designed modular edge membrane soil removal device ensures the successful recovery of the edge membrane after soil removal, a residual membrane recovery test was designed. The residual membrane recovery test was divided into two groups: one group installed with the modular edge membrane soil removal device, and the other group without the device. Each group of experiments was repeated 10 times, and the edge membrane recovery rate was calculated using Eq. (35), with the results averaged.

$$C = \frac{(m_0 - m_1)}{m_0} \tag{35}$$

In the equation: C is the edge membrane pickup rate (%); m_0 is the membrane mass before operation (g); m_1 is the membrane mass after operation (g).

5.2. Experimental Results and Analysis

The field experiment conditions are shown in Fig. 22, and the experimental results are presented in Table 9. The measured average soil removal rate is 92.38%, and the average lift height is 66.8 mm. The errors between these results and the simulation experiment results are all within 5%. The results indicate that the modular edge membrane soil removal device meets the operational requirements for residual membrane recovery and edge membrane removal.

Table 9. Test Results of the Edge-Lifting Film Device。

Region	Soil Remaining on the Membrane (g/dm²)	Pre-Test Soil Weight (g/dm²)	Soil Removal Rate (%)	Lift Height (mm)
A1	32.22	362.45	91.11	67.2
A2	14.07	422.36	96.67	67.1
A3	21.07	251.12	91.61	64.6
A4	26.62	356.34	92.53	68.1
A5	55.92	671.28	91.67	67.4
A6	28.65	429.77	93.33	65.1
A7	36.93	389.17	90.51	67.4
A8	36.33	425.95	91.47	68.8
A9	40.23	523.13	92.31	65.7
A10	28.22	379.42	92.56%	66.3

Figure 22. Field Test Results of the Edge-Lifting Film Device.

The field experiment conditions for edge membrane recovery are shown in *Fig. 23*, and the experimental results are presented in Table 10. In the area where the modular edge membrane soil removal device was installed, the edge membrane recovery rate was 94.82%. In the area without the modular edge membrane soil removal device, the residual membrane recovery rate was 88.24%. The experimental results demonstrate that installing the modular edge membrane soil removal device effectively increased the recovery rate of the edge membrane.

Table 10. Test Results of Edge Film Recovery.

Region	B1	B2
1	95.31	87.59
2	94.43	90.42
3	97.22	89.43
4	92.67	87.52
5	95.45	89.43
6	93.36	90.54
7	96.48	86.75
8	92.75	85.43
9	93.45	88.76
10	97.12	86.54
Mean Value	94.82	88.24

Figure 23. Field test results and measurement indicators for edge film recovery under different structural parameters.

6 Conclusions

(1) To address the issue of ineffective edge membrane flipping during residual film recovery, a modular soil removal and edge membrane lifting device was designed. A mechanical analysis of the edge membrane lifting device was conducted, and the main factors affecting operational performance were identified as the entry angle, rebate angle, and height difference.

(2) A discrete element simulation experiment of the edge membrane lifting device was performed, using the entry angle, rebate angle, and height difference as experimental factors, and the soil removal rate and lift height as performance indicators. The optimal parameter combination obtained was: entry angle 33.75°, rebate angle 47.9°, and height difference 135 mm. Under these parameters, the soil removal rate reached 94.6%, and the lift height was 68.5 mm.

(3) Field experiments were carried out for validation. The results showed that the average soil removal rate of the device was 92.38%, and the average lift height was 66.8 mm, which were consistent with the simulation results. The edge membrane recovery rate reached 94.82%, representing an improvement of 6.58 percentage points compared with the conventional residual film recovery machine without the edge membrane lifting device (recovery rate 88.24%). All performance indicators met the design requirements.

Author Contributions: Haojun Wen and Haixiao Gou; methodology, Haojun Wen, Hao Chen, and Zhaohui Zheng; validation, Xiaolong Yang and Minhui Song; data curation, Jie Zhang and Hao Chen; writing—original draft preparation, Haojun Wen and Hao Chen; writing—review and editing, Haixiao Gou and Zhaohui Zheng; funding acquisition, Haojun Wen. All authors have read and agreed to the published version of the manuscript.

Competing Interests: The authors declare no competing interests in this research.

Funding declaratuon: This research was supported by the National Key R&D Program of China (Project No. 2023YFD1701903).

Data Availability Statement: The original contributions presented in the study are included in the article; further inquiries can be directed to the corresponding author.

Conflicts of Interest: the research was conducted in the absence of any commercial or financial relationships that could be construed as a potential conflict of interest.

References

[1] Zhao, Y., Chen, X., Wen, H., Zheng, X., Niu, Q., & Kang, J. Research Status and Prospect of Control Technology for Residual Plastic Film Pollution in Farmland. *Trans. Chinese Soc. Agric. Mach.* **48**, 1–14 (2017).

[2] Jiang, D., Chen, X., Yan, L., et al. Research on Technology and Equipment for Resource Utilization of Farmland Residual Film. *Trans. Chinese Soc. Agric. Mach.* **41**, 179–190 (2020).

[3] Ma, S. Test and Analysis of Rolling Needle Residual Membrane Recovery Machine. *J. Tarim Univ.* **31**, 59–64 (2019).

[4] Wen, H. Investigation on the Research, Development, and Application of Mulching Film Recovery Machinery in Xinjiang. *Agric. Mach. Technol. Extens.* **2024**, 9–11 (2024).

[5] Zhuansun, Y., Wang, Y., Cai, J., et al. Research Status of Residual Film Recovery Machines in China. *Southern Agric. Mach.* **53**, 48–50 (2022).

[6] Jin, W. Review of Recycling Technology and Equipment of Plastic Film Mulch. *Southern Agric. Mach.* **51**, 72–73 (2020).

[7] Wittwer, S. H. World-wide Use of Plastics in Horticultural Production. *Hort. Technol.* **3**, 6–19 (1993).

[8] Xie, J., Yang, Y., Tang, W. Performance Analysis and Test of Different Rising Edge Film Devices Based on Discrete Element Method. *J. Agric. Mech. Res.* **43**, 10–17 (2021).

[9] Zhang, J., Zhang, L., Liu, X. Mechanical Analysis and Contrast Experiment on Collecting Residual Plastic Film with Different Side-film Shovels. *Trans. Chinese Soc. Agric. Eng.* **33**, 10–15 (2017).

[10] Han, Y., Xu, Y., Sun, L. Design and Analysis of Edge Film Recovery Mechanism Based on Finite Element Method. *Southern Agric. Mach.* **55**, 122–125 (2024).

[11] Hu, G., Quan, L., Zou, Y. Design and Experiment of Devices for Soil-Crushing for Recovery of Edge Film from Ridge Planting Residual Film. *J. Gansu Agric. Univ.* **56**, 190–198 (2021).

[12] Ma, S., Zhang, X. Design and Experiment of Side Used Plastic Film Collector Machine. *Agric. Eng.* **28**, 73–75 (2012).

[13] Jiang, Y., Qu, H., Liu, X. Design and Simulation of Spade Tooth Film Lifting Device for Residual Film Recycling Machine. *Trans. Chinese Soc. Agric. Mach.* **(preprint)**, 1–10 (2025).

[14] Zhao, Y., Zheng, X., Chen, X. Design and Test of CMJY-1500 Type Plastic Film Residue Collecting and Balling Machine. *Trans. Chinese Soc. Agric. Eng.* **33**, 1–9 (2017).

[15] Yi, F., Shi, J., Yang, G. Study and Application of Mouldboard Plough. *J. Chin. Agric. Mech.* **40**, 231–236 (2019).

[16] Dai, P., Zhao, X., Si, B. High-Speed Plow Body Surface Structure Normalized Design and Modal Analysis. *J. Dyn. Control* **20**, 10–23 (2022).

[17] Wang, D. Research on Parametric Design of the Fire-Fighting Plow Moldboard Surface. PhD Thesis, Nanjing Forestry University, 2006.

[18] Chen, Z. *Agricultural Machinery Design Handbook*; China Agricultural Mechanization Science Research Institute: Beijing, China, 2007; pp. 188–200, 568–585, 1104–1105.

[19] He, Z., Yang, F., Sun, H. On Parametric Design of Horizontal Straight Generatrix Plough Body Surface. *Mech. Sci. Technol.* **2002**, 562–564 (2002).

[20] Yang, H., Liu, L. Parametric Design of Horizontal Straight Generatrix Plough Body Surface Based on SolidWorks. *Agric. Equip. Veh. Eng.* **2008**, 22–26 (2008).

[21] Gong, H. Dynamic Analysis of Submarine Ploughing Machine and Moldboard Surface Optimization. PhD Thesis, Harbin Engineering University, 2014.

[22] Zhao, Y., Wang, W., Liu, J. Three-dimensional Parametric Design of Horizontal Straight Generatrix Plough Body Surface. *J. Agric. Mech. Res.* **33**, 89–91 (2007).

[23] Park, S., Zhang, Q., Liu, H., et al. Design and Simulation Experiment on Double-Wing Deep Subsoiler Based on EDEM. *Guangdong Agric. Sci.* **41**, 182–186 (2014).

[24] Zhen, W., Yang, D., Huang, S. Experimental Study on a Type of Subsoiling Shovel with Flank. *J. Agric. Mech. Res.* **33**, 119–122 (2011).

[25] Xue, H., Yang, L., Lian, D., et al. Tests of Designing Parameters of Double-Wing Subsoiler. *J. Northwest A&F Univ.* **(Nat. Sci. Ed.) 33**, 24–29 (1987).

[26] Ma, T., Ye, Y. Prediction of the Trajectory of Soil Motion on the Moldboard Plow Surface. *Trans. Chinese Soc. Agric. Mach.* **S1**, 5–8 (1996).

[27] Pang, J., Liu, X., Chen, S., et al. Study on Measurement and Calibration Methods of Soil Parameters Used in Discrete Element Method. *Anhui Agric. Sci.* **51**, 6–11 (2023).

[28] Ye, D., Lin, Z., Qing, J. Discrete Element Parameter Calibration of Soil-Touching Parts of Fungus in Transplanting Under Typical Moisture Content. *China Agric. Mech.* **(preprint)**, 1–10 (2024).

[29] Hu, G., Quan, L., Zou, Y., et al. Establishment and Simulation Experiment of the Membrane-Soil Separation Model for the Mechanical Recovery of Residual Membrane in Farmland. *J. Hunan Agric. Univ. (Nat. Sci.)* **47**, 344–350 (2021).

[30] Shen, S., Zhang, J., Jiang, Y., et al. Tensile Properties of Residual Film in Tillage Layer Based on Discrete Element Method. *Trans. Chinese Soc. Agric. Mach.* **55**, 132–141 (2024).

[31] Jin, W., Zhang, X., Ding, Y., et al. Experiment on Suspension Separation of Residual Film and Impurity Based on EDEM Fluent Coupling. *Trans. Chinese Soc. Agric. Mach.* **53**, 89–98 (2022).

[32] Yang, Y. Design and Experiment of Guide Chain Harrow-Type Residual Membrane Recovery Machine. PhD Thesis, Xinjiang Agricultural University, 2022.

[33] Jiang, D. Research and Experiment on the Clean-Up System of Follow-up Residual Membrane Recovery Machine. PhD Thesis, Shihezi University, 2020.

[34] Deng, H., Dai, F., Shi, R., et al. Simulation and Test on the Operation Process of an Intermittent Film-Picking Component on Full-Film Mulched Double Ditches. *Biosyst. Eng.* **239**, 190–206 (2024).

[35] Jin, Z. Simulation and Experiment of Soil Removal Device for Corn Straw Picking and Pelletizing Machine. PhD Thesis, Shenyang Agricultural University, 2021.